

# Naturally Occurring 2D Heterostructure Nagyágite with Anisotropic Optical Properties

Arindam Dasgupta, Jie Gao,\* and Xiaodong Yang\*

**Nagyágite is a naturally occurring layered van der Waals heterostructure composed of alternating layers of [Pb(Pb,Sb)S<sub>2</sub>] and [(Au,Te)], where the component lattices are commensurately modulated. The weak van der Waals stacking between the heterolayers facilitates mechanical exfoliation. Due to its monoclinic crystal structure, nagyágite exhibits structural anisotropy which induces strong optical anisotropy. Here, the anisotropic optical properties of ultrathin nagyágite flakes mechanically exfoliated from a natural mineral are demonstrated through angle-resolved polarized Raman scattering, linear dichroism, and polarization-dependent anisotropic third-harmonic generation. The study establishes nagyágite as a new type of natural van der Waals heterostructure based 2D material, which can be exploited for realizing ultrathin anisotropic optical devices for future on-chip photonic integrated circuits.**

a wide range of applications under the umbrella of one single material.<sup>[9–14]</sup> In addition to the focused direction of the artificial stacking of 2D material layers to fabricate heterostructures, the exfoliation of natural layered minerals consisting of alternating material building blocks has also come into the foray as an efficient way of creating ultrathin vdW heterostructures. Recently, it has been demonstrated that natural vdW minerals such as franckeite<sup>[15–17]</sup> and cylindrite<sup>[18]</sup> composed of alternating PbS- and SnS<sub>2</sub>-like layers can be exfoliated to a few layer thicknesses for realizing diverse optoelectronic and optical applications such as photodetection, linear dichroism, nonlinear harmonic generation,<sup>[19]</sup> and large Kerr nonlinearity.<sup>[20]</sup>

## 1. Introduction


The studies on 2D materials are one of the most interesting topics in modern day scientific research. The confinement of charge carriers, phonons, and photons in the 2D planes of these materials leads to remarkable changes in the electronic and optical properties.<sup>[1–3]</sup> Recently discovered 2D materials such as graphene, black-phosphorus, and transition-metal dichalcogenides have rapidly expanded the use of 2D materials for developing numerous innovative technologies and applications.<sup>[4–8]</sup> Furthermore, the ultrathin thickness of the 2D geometry facilitates the 2D materials to be integrated with traditional electronic and photonic materials for future on-chip devices. Therefore, exploring new layered 2D materials with weak van der Waals (vdW) bonding has recently become a subject of intense research in further expanding the family of 2D materials. Going beyond the traditional materials, heterostructures formed by distinct vdW stacking of different 2D materials also feature fascinating physical properties and facilitate

However, the complex superlattices exhibit strain induced deformation due to incommensurability between the alternative layers. Therefore, understanding the detailed crystal structure and fundamental properties of these incommensurate vdW materials are a challenging job. Apart from the natural vdW heterostructures belonging to the cylindrite and franckeite family, there are other layered minerals where the heterostructures are composed of commensurately modulated alternative layers, for example, nagyágite [Pb<sub>2</sub>(Pb,Sb)<sub>2</sub>S<sub>4</sub>][(Au,Te)<sub>2</sub>], buckhornite [Pb<sub>2</sub>BiS<sub>3</sub>][AuTe<sub>2</sub>]<sup>[21,22]</sup> and jaszczakite [(Bi,Pb)<sub>3</sub>S<sub>3</sub>][AuS<sub>2</sub>]<sup>[23]</sup> to name a few. Nagyágite is one naturally occurring sulpho-telluride mineral of lead, antimony and gold, occurring in gold-tellurium epithermal hydrothermal veins, which was named by Hadinger in 1845 after the type locality of Nagyág (now Săcărâmb) in Romania<sup>[24,25]</sup> The layered heterostructure of nagyágite is composed of weakly coupled alternating [Pb(Pb,Sb)S<sub>2</sub>] rocksalt layers and single-atom thick [(Au,Te)] sheets, where the charge carriers are naturally confined in atomically thin [(Au,Te)] sheets. Unlike franckeite and cylindrite, the adjacent heterolayers in nagyágite are perfectly commensurable with each other. Recently, synthetic nagyágite crystals with a thickness of 50 μm have been reported to show high room-temperature electron mobility and large transverse nonsaturating negative magnetoresistance.<sup>[26]</sup> However, as a layered mineral, till-date there has been no study on the exfoliation of naturally occurring nagyágite crystals. Also, as a monoclinic layered crystal, the anisotropic optical properties of nagyágite have not been studied yet.

Here, we show that naturally occurring nagyágite crystals can be mechanically exfoliated to fabricate ultrathin vdW heterostructures. By performing transmission electron microscopy (TEM), energy-dispersive X-ray spectroscopy (EDXS), and X-ray

A. Dasgupta, J. Gao, X. Yang  
Department of Mechanical and Aerospace Engineering  
Missouri University of Science and Technology  
Rolla, MO 65409, USA  
E-mail: jie.gao.5@stonybrook.edu; yangxia@mst.edu

J. Gao  
Department of Mechanical Engineering  
Stony Brook University  
Stony Brook, NY 11794, USA

 The ORCID identification number(s) for the author(s) of this article can be found under <https://doi.org/10.1002/admi.202101106>.

DOI: 10.1002/admi.202101106

photoelectron spectroscopy (XPS) analysis, we first determine the crystal structure and chemical composition of the exfoliated nagyágite flakes. The in-plane structural anisotropy in the crystal is further demonstrated using angle-resolved polarized Raman spectroscopy. Furthermore, by performing polarization-dependent absorption measurements, we demonstrate that the optical anisotropy in the crystal results in distinct linear dichroism in thin nagyágite flakes. Finally, we show that the exfoliated nagyágite flakes exhibit anisotropic third-harmonic generation (THG), which can be utilized for determining the crystal axes. Our results introduce nagyágite as a natural vdW heterostructure which can be exfoliated to 2D form. Moreover, these results not only provide a better understanding of the anisotropic light-matter interaction present in the material, but also can be harnessed to realize ultrathin anisotropic optical devices such as polarization-sensitive photodetectors, optical modulators and nonlinear beam converters for future on-chip photonic circuits.

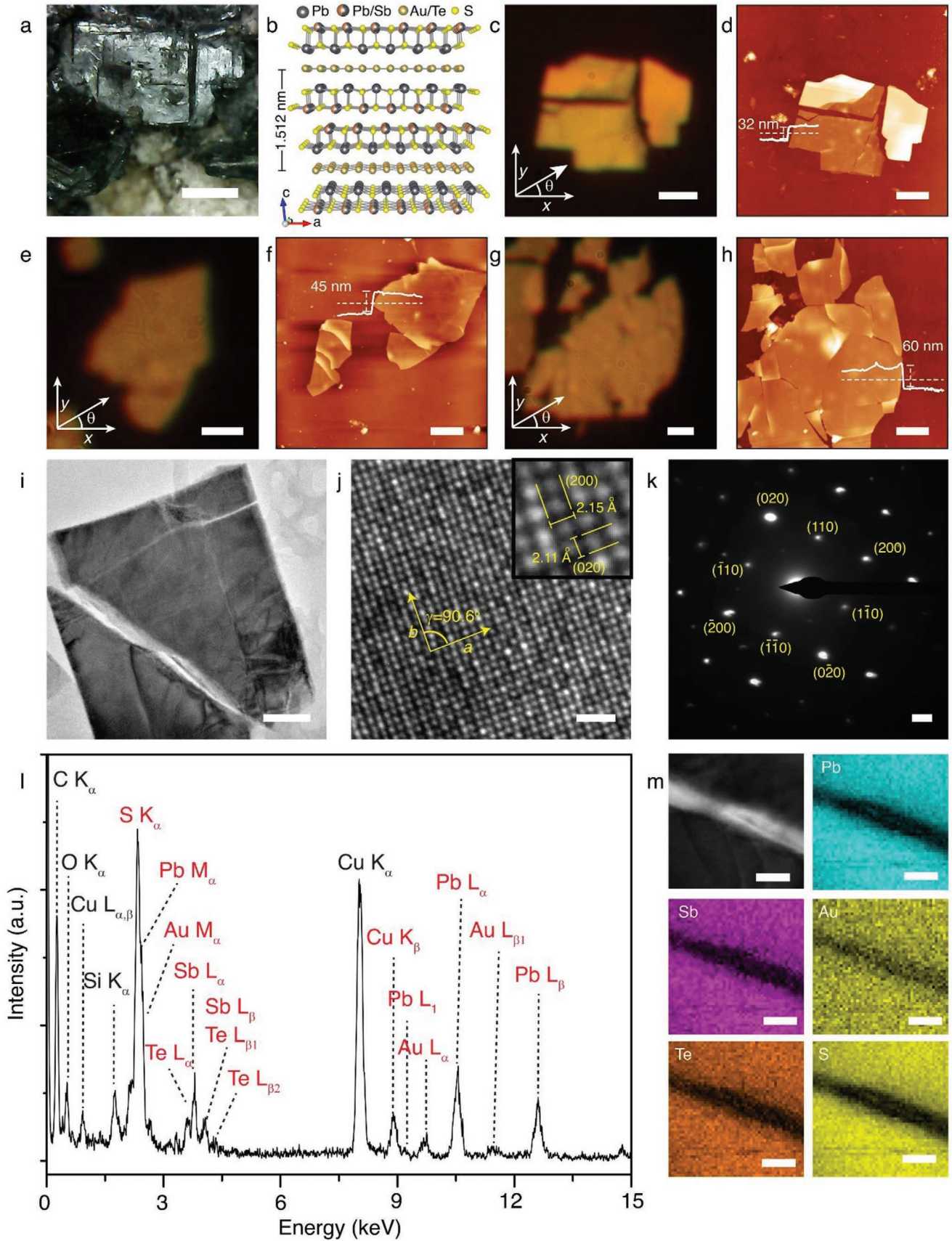
## 2. Results and Discussion

### 2.1. Mechanical Exfoliation, Chemical Composition, and Surface Characterization of Nagyágite Crystal

Figure 1a shows the reflection image of a nagyágite mineral rock acquired from Săcărâmb, Deva, Hunedoara, Romania, where thin platy crystals of nagyágite with blackish lead-gray color on white calcite are visible. Figure 1b is the schematic representation of the crystal structure of nagyágite, in which the heterostructure consists of alternating stacks of weakly coupled  $[\text{Pb}(\text{Pb},\text{Sb})\text{S}_2]$  layers and single-atom thick  $[(\text{Au},\text{Te})]$  sheets along the  $c$ -axis. Two slices of  $[\text{Pb}(\text{Pb},\text{Sb})\text{S}_2]$  form one pair of distorted PbS-archetype layers of four atomic sheets thick, where Sb atoms are selectively mixed in the Pb sites of the slices facing each other, while the sites facing the  $[(\text{Au},\text{Te})]$  sheets are fully occupied by Pb atoms. The single-atom thick planar square nets of disordered Au and Te atoms are sandwiched between the distorted PbS-archetype layers. Nagyágite exhibits close structural relationship to another member of a homologous series, buckhornite, in which two  $(\text{Pb},\text{Bi})\text{S}$  atomic sheets form one PbS-archetype layer separated between the gold-tellurium sheets<sup>[21,22]</sup> While for jaszczakite, being the S-Bi-analogue of buckhornite, gold-sulfide sheets are formed instead.<sup>[23]</sup> Nagyágite has a monoclinic crystal structure belonging to the  $P2_1/m$  space group. The unit cell parameters are determined as,  $a = 4.22 \text{ \AA}$ ,  $b = 4.18 \text{ \AA}$ , and in the stacking direction the layer pairs are repeated at a period of  $c = 15.12 \text{ \AA}$ , while  $\alpha = \gamma = 90^\circ$  and  $\beta = 95.42^\circ$ .<sup>[27]</sup> The lattice shift between the two PbS-archetype slices of  $[\text{Pb}(\text{Pb},\text{Sb})\text{S}_2]$  along the  $a$ -direction of the crystal is mainly responsible for the deviation of the average unit cell from the orthogonal metrics of PbS-like crystal and thereby induces structural anisotropy in the  $a$ - $b$  plane. Weak vdW stacking between the adjacent layers facilitates mechanical exfoliation of nagyágite. We exfoliate bulk nagyágite minerals using Nitto tape (SPV 224) to obtain thin flakes with different thicknesses on quartz substrate. Figure 1c is the reflection microscope image of one exfoliated flake. The associated atomic force microscopy (AFM) image in Figure 1d shows the surface topology of the flake. From the height profile in the inset of

AFM image, the thickness of the flake is estimated to be 32 nm. Figure 1e-h shows the reflection microscope images and AFM images of other two exfoliated flakes with thicknesses of 45 and 60 nm, respectively. Figure 1i is a low-magnification TEM image of a mechanically exfoliated nagyágite flake on copper TEM grid. The atomic arrangement of the crystal is visible in the high-resolution TEM (HRTEM) image in Figure 1j. No presence of interlayer moiré fringes which generally arises from the local atomic alignment between the stacked layers in vdW heterostructures further indicates perfect commensuration between the constituent  $(\text{Pb},\text{Sb})\text{S}$ - and  $(\text{Au},\text{Te})$ -type layers. The magnified view of the atomic arrangement in the HRTEM image in the inset of Figure 1j further shows that the lattice spacings of the  $(200)$  and  $(020)$  sets of planes are 2.15 and 2.11 Å, respectively. The intersection angle between these two sets of planes is  $90.6^\circ$ . Therefore, the lattice parameters in the  $a$ - $b$  plane are  $a = 4.30 \text{ \AA}$ ,  $b = 4.22 \text{ \AA}$ , and  $\gamma = 90.6^\circ$  for the current natural nagyágite crystal, which are more or less close to the previously determined lattice parameters of  $a = 4.22 \text{ \AA}$ ,  $b = 4.18 \text{ \AA}$ , and  $\gamma = 90^\circ$  for one synthetic nagyágite crystal,<sup>[27]</sup> as well as  $a = 4.17 \text{ \AA}$ ,  $b = 4.15 \text{ \AA}$ , and  $\gamma = 90^\circ$  for another synthetic nagyágite.<sup>[26]</sup> The selected area electron diffraction (SAED) pattern along the surface normal to the  $[001]$  crystal zone axis is shown in Figure 1k. It should be noted that due to the commensuration between the constituent lattices of the nagyágite crystal, the generated spot patterns from individual layers are identical. To analyze the chemical composition of the exfoliated nagyágite flakes, we performed EDXS analysis. Figure 1l is the averaged EDXS spectrum obtained from a nagyágite flake, which confirms the existence of the main elements Pb, Sb, S, Au, and Te. The EDXS mapping of the individual elements from the area shown in the bright-field TEM image in Figure 1m indicates the uniform distribution of each element in the crystal, when viewed along the  $[001]$  crystal zone axis. The chemical stoichiometry of the individual heterolayers is also calculated from the EDXS results. The ratio between the Pb, Sb, and S is observed to be 2.76:1.19:4, while the ratio between Au and Te is obtained to be 1:2.8. Therefore, the approximate chemical formula is determined as  $[(\text{Pb}_{2.76}\text{Sb}_{1.19})_{\Sigma=3.95}\text{S}_4][(\text{Au}_{0.63}\text{Te}_{1.77})_{\Sigma=2.4}]$ . Although the calculated formula is close to that of the actual formula of nagyágite, a slight overestimation in the quantity of Au and Te may be attributed to the heavy overlap between Pb  $M_{\alpha}$ , Au  $M_{\alpha}$ , and S  $K_{\alpha}$  peaks, as well as between Sb and Te peaks. The presence of Cu peak in the EDXS spectrum is due to the copper TEM grid, whereas Si, C and O peaks may be arising from the underlying carbon film of the copper TEM grid and the presence of carbon adsorbents accumulated on the crystals during their polymethyl methacrylate (PMMA)-assisted transfer of the crystals on the grid.

The surface oxidation and stability of the exfoliated nagyágite flakes are investigated through XPS analysis. Figure 2a shows the averaged XPS survey spectrum obtained from air-aged nagyágite crystal. The XPS peaks of all the major elements can be observed. Absence of any oxygen peak in the XPS spectrum suggests that the exfoliated nagyágite crystals are stable in ambient condition. Further, the oxidation states of each element are determined from the XPS results. Figure 2b-f are the high-resolution spectra around Pb 4f, Sb 3d, Te 3d, Au 4f, and S 2p regions. Pb is present in the crystal at 2+ and 4+ states





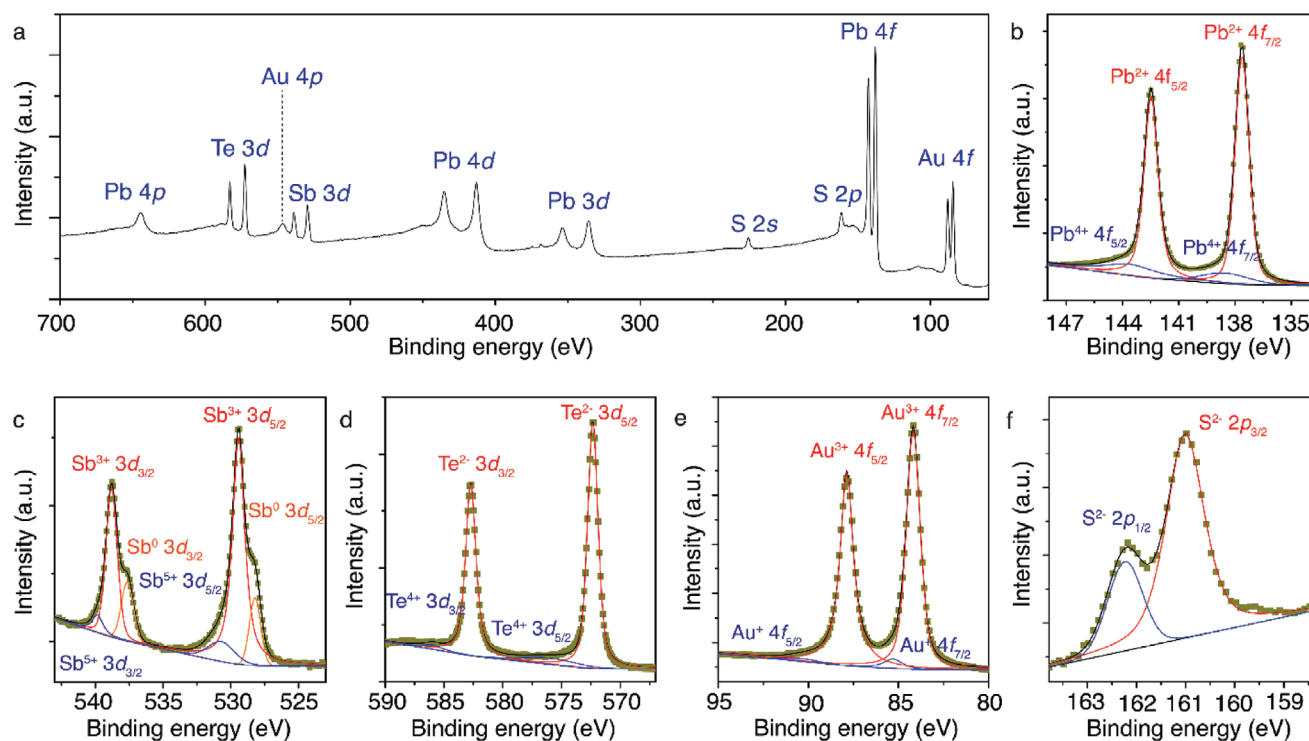


**Figure 2.** a) XPS survey spectrum from nagyágite crystal. b–f) High-resolution spectra around the Pb 4f, Sb 3d, Te 3d, and S 2p binding energy regions.

at 83% and 17% ratio. While most of the Sb atoms are present at 3+ (72%) and 5+ (10%) states, a considerable quantity (18%) is observed to be at 0 oxidation state. 92% of the Te atoms are found to be at 2- oxidation state, while 8% are at 4+ state. 91% of Au is present at 3+ state, while S is solely present at 2- state.

## 2.2. Polarization-Resolved Raman Spectroscopy of Nagyágite Flakes

First, we determine the structural anisotropy in the exfoliated nagyágite flakes using Raman spectroscopy. The Raman spectrum from the 32 nm thick nagyágite flake (Figure 1c) is shown in Figure 3a which is acquired by exciting the flake with a 632 nm wavelength He-Ne laser. The Raman spectrum of nagyágite exhibits several distinct Raman peaks within the spectral range of 70–400  $\text{cm}^{-1}$ , which are located at 78, 137, 182, 205, 252, 284, and 319  $\text{cm}^{-1}$ . The Raman modes of nagyágite can be assigned according to the Raman spectra of the constituent components, including galena  $\text{PbS}$ ,<sup>[28]</sup> stibnite  $\text{Sb}_2\text{S}_3$ ,<sup>[29,30]</sup> and calaverite  $\text{AuTe}_2$ . The 78  $\text{cm}^{-1}$  peak is assigned as the  $A_g$  mode

of  $\text{Sb}_2\text{S}_3$  (73  $\text{cm}^{-1}$ ). The 137  $\text{cm}^{-1}$  peak is related to the transverse acoustic and optical phonon modes of  $\text{PbS}$  lattices (154  $\text{cm}^{-1}$ ) and the Raman mode of  $\text{AuTe}_2$  (155  $\text{cm}^{-1}$ ). The 182  $\text{cm}^{-1}$  peak is assigned as the  $A_g$  mode of  $\text{Sb}_2\text{S}_3$  (191  $\text{cm}^{-1}$ ). The peak at 205  $\text{cm}^{-1}$  is attributed to the longitudinal optical phonon modes of  $\text{PbS}$  lattices (204  $\text{cm}^{-1}$ ). The 252  $\text{cm}^{-1}$  peak represents a combination of the  $B_{1g}/B_{3g}$  mode of  $\text{Sb}_2\text{S}_3$  (238  $\text{cm}^{-1}$ ) and the broad Raman shift of  $\text{AuTe}_2$  at about 230  $\text{cm}^{-1}$  (190–270  $\text{cm}^{-1}$ ). The two peaks at 284 and 319  $\text{cm}^{-1}$  are assigned as the  $A_g$  modes of  $\text{Sb}_2\text{S}_3$  (283 and 312  $\text{cm}^{-1}$ ).

The lattice orientation of the anisotropic crystal system of nagyágite can be determined through angle-resolved polarized Raman spectroscopy. Previously, this technique has been used for other monoclinic crystal systems such as  $\text{GeAs}$ <sup>[31]</sup> and  $\text{MoTe}_2$ .<sup>[32]</sup> Figure 3b,c are contour color maps of the Raman intensity variation of the parallel and perpendicular polarization components as a function of the incident polarization angle ( $\theta$ ) with respect to the  $x$ -axis ( $\theta = 0^\circ$ ). These maps further confirm the presence of  $A_g$  modes at 137, 182, 191, 205, and 319  $\text{cm}^{-1}$  and  $B_g$  mode at 252  $\text{cm}^{-1}$ . To gain more detailed understanding of the polarization-dependent Raman scattering characteristics,

**Figure 1.** a) Reflection image of the nagyágite mineral rock where many blackish-lead gray colored thin platy crystals are naturally formed on white calcite. Scale bar is 2 mm. b) Schematic diagram of the side view of nagyágite crystal showing that the crystal is made of alternating layers of  $[\text{Pb}(\text{Pb},\text{Sb})\text{S}_2]$  and  $[(\text{Au},\text{Te})]$ . c) Reflection microscope image of a mechanically exfoliated nagyágite crystal. d) AFM image showing the surface topography of the crystal, where the line profile in the inset shows that the flake is 32 nm thick. Scale bars are 2  $\mu\text{m}$ . e, g) Reflection microscope images and f, h) AFM images of other two nagyágite flakes with thicknesses of 45 and 60 nm. Scale bars are 2  $\mu\text{m}$ . i) Low-magnification TEM image of an exfoliated nagyágite flake on copper TEM grid. Scale bar is 200 nm. j) HRTEM image of the flake showing the atomic arrangement. Scale bar is 1 nm. Inset is a magnified view of a section of the image, where the distance between atoms corresponding to each  $(h,k,l)$  plane is measured. k) Corresponding SAED pattern. Scale bar is 1  $\text{nm}^{-1}$ . l) Acquired EDXS spectrum from the nagyágite flake. m) TEM-EDXS map of the main elements Pb, Sb, Au, Te, and S from the area of the nagyágite flake shown in the bright-field TEM image. Scale bars are 50 nm.

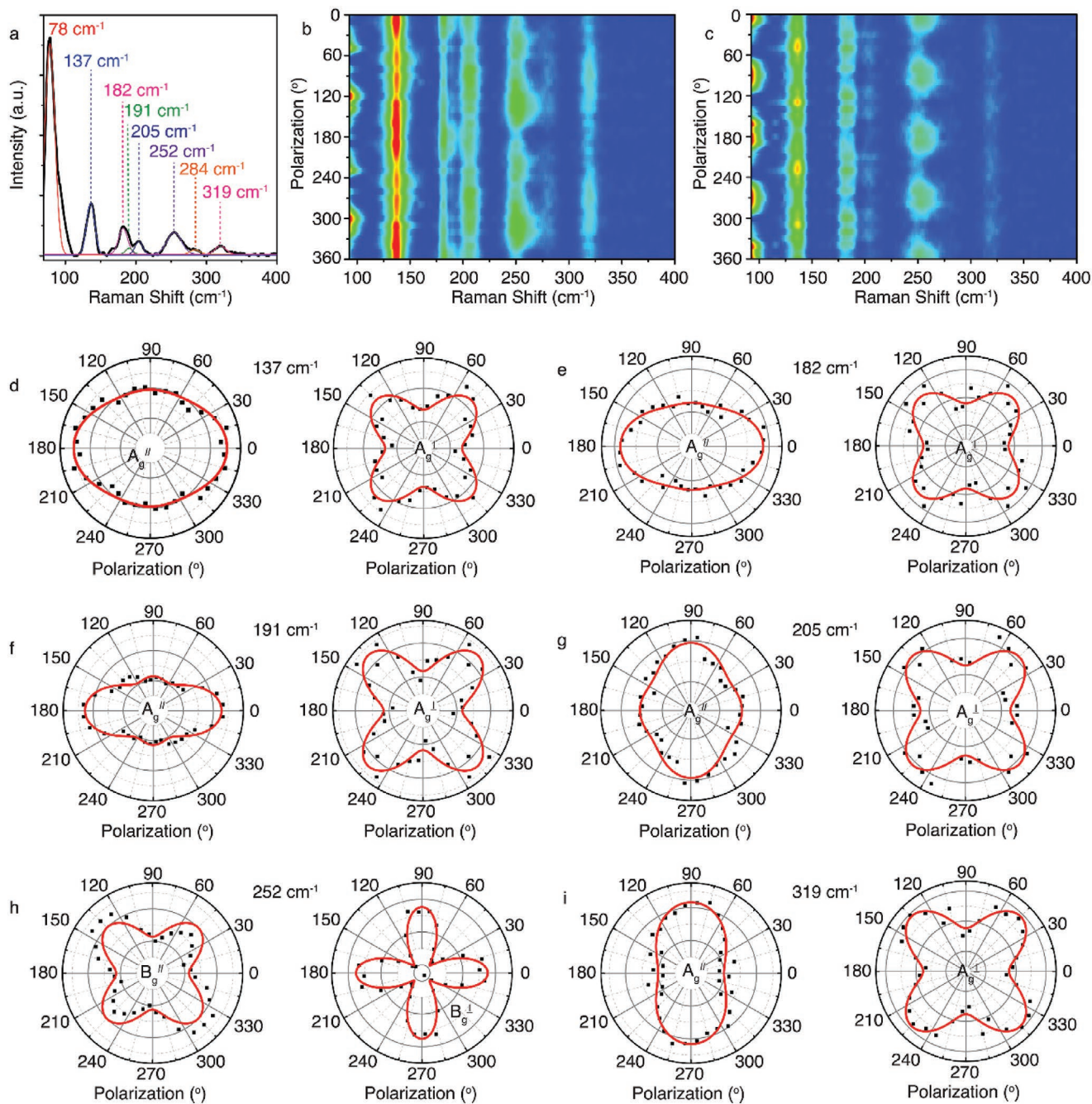


**Figure 3.** a) Raman spectrum acquired from the 32 nm thick nagyágite flake with the fitted curve for each Raman peak. b,c) Contour color maps of the parallel and perpendicular polarization components of Raman spectra as a function of the incident polarization angle. d–g,i) Polar plots of the Raman intensity variation of the parallel and perpendicular polarization components for the  $A_g$  modes at 137, 182, 191, 205, and 319  $\text{cm}^{-1}$ . h) Polar plot of the Raman intensity variation for the  $B_g$  mode at 252  $\text{cm}^{-1}$ .

the intensity variation of each mode is fitted with a Raman tensor. By considering the monoclinic crystal structure of nagyágite belonging to space group  $P2_1/m$ , the Raman tensors for the  $A_g$  and  $B_g$  modes can be written as

$$\overleftrightarrow{R}_{A_g} = \begin{pmatrix} a & 0 & d \\ 0 & b & 0 \\ d & 0 & c \end{pmatrix} \quad (1)$$

$$\overleftrightarrow{R}_{B_g} = \begin{pmatrix} 0 & f & 0 \\ f & 0 & g \\ 0 & g & 0 \end{pmatrix} \quad (2)$$

where  $a$ ,  $b$ ,  $c$ ,  $d$ ,  $f$ , and  $g$  are components of the Raman tensors. Mostly, these components are treated as real values since the imaginary part of the Raman susceptibility is negligible

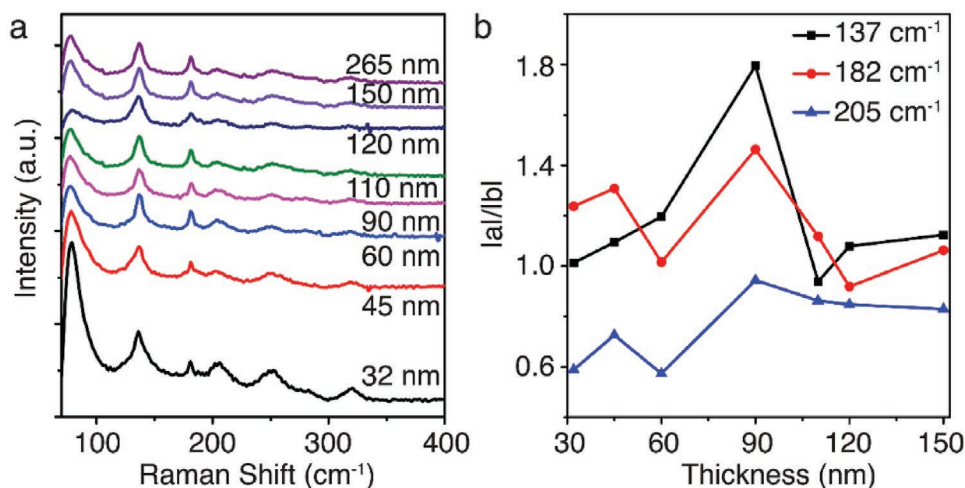


**Figure 4.** a) Raman spectra from nagyágite flakes of different thicknesses. No Raman shift variation is observed depending on the flake thickness. b) Evolution of the anisotropy ratios of Raman tensor components  $|a|/|b|$  for three different  $A_g$  modes at 137, 182, and 205  $\text{cm}^{-1}$  as a function of the flake thickness.

in transparent materials. However, for flakes with significant absorption, the components are complex elements, and can be represented as  $R_{ij} = |R_{ij}| e^{i\phi_{R_{ij}}}$ . The Raman intensity is thus calculated as  $I = |\hat{\epsilon}_s \cdot R \cdot \hat{\epsilon}_i|^2$ , where the unit polarization of the incident beam is  $\hat{\epsilon}_i = [\cos\theta \ \sin\theta \ 0]$ , and the unit polarization of the scattered beam is expressed as  $\hat{\epsilon}_s = [\cos\theta \ \sin\theta \ 0]$  and  $\hat{\epsilon}_s = [-\sin\theta \ \cos\theta \ 0]$  for the parallel and perpendicular polarizations, respectively. Therefore, the angle-dependent Raman intensities of the parallel and perpendicular polarization components of the  $A_g$  and  $B_g$  modes can be written as

$$I_{\parallel}(A_g) \propto |a|^2 \cos^4 \theta + |b|^2 \sin^4 \theta + \frac{|a||b|}{2} \cos \phi_{ab} \sin^2 2\theta \quad (3)$$

$$I_{\perp}(A_g) \propto \frac{1}{4} (|a|^2 + |b|^2 - 2|a||b| \cos \phi_{ab}) \sin^2 2\theta \quad (4)$$

$$I_{\parallel}(B_g) \propto |f|^2 \sin^2 2\theta \quad (5)$$

$$I_{\perp}(B_g) \propto |f|^2 \cos^2 2\theta \quad (6)$$

where  $\phi_{ab}$  is the phase difference between  $a$  and  $b$ . Figure 3d–g,i are polar plots of the Raman intensity variation of the parallel and perpendicular polarization components for the  $A_g$  modes at 137, 182, 191, 205, and 319  $\text{cm}^{-1}$  as a function of the incident polarization angle. The parallel components of most of the  $A_g$  modes are found to exhibit a four-lobe pattern with two unequal maxima perpendicular to each other. As reported for other monoclinic crystals belonging to the same space group, such as  $\text{MoTe}_2$ , the orientation of these maxima signifies the crystal axes ( $a$ - or  $b$ -axis). The presence of the secondary maxima indicates that the phase term  $\phi_{ab}$  is important and there is a significant amount of absorption present in the crystal. The principal maxima of the Raman intensity variation of the parallel components for the  $A_g$  modes at 137, 182, and 191  $\text{cm}^{-1}$  are oriented along  $\theta = 0^\circ$ , while for the  $A_g$  modes at 205 and 319  $\text{cm}^{-1}$ , the principal maxima are oriented along  $\theta = 90^\circ$ . Therefore, it can be inferred that the directions of  $\theta = 0^\circ$

and  $90^\circ$  are either the crystal's  $a$ - or  $b$ -axis. The Raman intensity variation of the perpendicular components of all the  $A_g$  modes shows a symmetric four-lobe pattern with the intensity minima occurring for the incident polarization being along either of the crystal's  $a$ - or  $b$ -axis. Figure 3h plots the angle-dependent evolution of the Raman intensity of the  $B_g$  mode at 252  $\text{cm}^{-1}$  as a function of the incident polarization angle. As expected from Equations (5) and (6), both the parallel and perpendicular polarization components exhibit a symmetric four-lobe pattern, where the intensity minima and maxima are preferential to the incident polarization being along one of the crystal's axes in respective cases.

According to Equation (3), the ratio of Raman intensity  $I_{\parallel}(A_g)_{\theta=0^\circ} / I_{\parallel}(A_g)_{\theta=90^\circ}$  underlines the  $|a|^2/|b|^2$  ratio, which reflects the in-plane Raman scattering anisotropy of the nagyágite crystal. Based on the semi-classical model of Raman scattering process,<sup>[33,34]</sup> the Raman tensor components  $a$  and  $b$  are described by the derivatives of the dielectric constant components  $\epsilon_{xx}$  and  $\epsilon_{yy}$  of nagyágite with respect to the vibrational normal coordinates  $q$  of the corresponding  $A_g$  mode, as  $a = \partial\epsilon_{xx} / \partial q^{A_g}$  and  $b = \partial\epsilon_{yy} / \partial q^{A_g}$ , respectively. It is found that the anisotropy ratios of Raman tensor components  $|a|/|b|$  for three different  $A_g$  modes at 137, 182, and 205  $\text{cm}^{-1}$  are 1.01, 1.24, and 0.59 for the 32 nm thick flake, respectively, manifesting that the modulation strengths of the dielectric constant components  $\epsilon_{xx}$  and  $\epsilon_{yy}$  along two crystal's axes by the specific  $A_g$  phonon modes are not equal. In addition, the difference between  $\epsilon_{xx}$  and  $\epsilon_{yy}$  is also associated with the linear dichroism of nagyágite. The obtained anisotropic Raman tensor further indicates the anisotropic electron-photon and electron-phonon interactions in the nagyágite crystal.

Furthermore, the flake thickness dependence of the Raman modes is also explored. Figure 4a plots the obtained Raman spectra of the parallel polarization components from eight flakes of thicknesses ranging between 30–270 nm. No obvious variation in the Raman shifts of all  $A_g$  and  $B_g$  modes depending on the thickness is observed, due to the commensurate stacking of the constituent (Pb,Sb)S- and (Au,Te)-type layers in



the nagyágite crystal. To understand the thickness dependence of the anisotropy in the Raman tensor components, the  $|a|/|b|$  ratio is measured for all the flakes for three different  $A_g$  modes at 137, 182, and 205  $\text{cm}^{-1}$ , as plotted in Figure 4b. It shows that the  $|a|/|b|$  ratio for the Raman mode at 205  $\text{cm}^{-1}$  is always less than 1, which increases from 0.59 for the 32 nm flake almost to a stable value of 0.83 as the flake thickness increases up to 150 nm. On the contrary, the  $|a|/|b|$  ratios for the 137 and 182  $\text{cm}^{-1}$  modes are mostly larger than 1 with the peak values of 1.79 and 1.46 for the 90 nm flake, respectively, although there are some oscillations as a function of the flake thickness. It indicates that the Raman scattering anisotropy can be opposite for different Raman  $A_g$  modes, while the change of the  $|a|/|b|$  ratio depending on the flake thickness is probably attributed to the variation of dielectric constant property for thin nagyágite flakes as compared to that of the bulk crystal.

### 2.3. Linear Dichroism in Nagyágite Flake

Next, we explore the anisotropic optical properties of the thin nagyágite flake of 32 nm thickness (Figure 1c) by performing polarization-dependent absorption measurements. Figure 5a plots the measured reflectance ( $R$ ), transmittance ( $T$ ), absorbance ( $A$ ) spectra in the 430–800 nm wavelength range when the incident white light is linearly polarized along the  $x$  direction at

$\theta = 0^\circ$ . The reflectance response shows a peak around 490 nm, while the transmittance increases gradually as a function of wavelength after showing a deep around 510 nm. This justifies the greenish yellow color of the crystal observed in the reflection image. The absorbance is calculated from the measured reflectance and transmittance using the relationship  $A = 1 - R - T$ . The absorbance response remains nearly flat in the wavelength range of 430–800 nm, while showing a slowly decreasing trend with increasing wavelength, suggesting the possibility that nagyágite has a narrow band gap much lower than 1.55 eV. A previous study on synthetic nagyágite revealed that it has high electron mobility and hence a very narrow band gap.<sup>[26]</sup> Low-temperature resistivity measurement revealed that the resistivity of the material increases with decreasing temperature, indicating semiconducting behavior. However, no obvious band gap above 0.05 eV was observed even in electronic absorption spectroscopy, due to the interference from free carriers in nagyágite. The effect of the quartz substrate is further investigated by monitoring the reflectance, transmittance, and absorbance spectra from bare quartz substrate, as plotted in Figure 5a. It is clear that the absorption of the quartz substrate is negligible compared to that of the nagyágite flake. In Figure 5b, a series of absorbance spectra are plotted for different incident linear polarization angles. We observe that the absorbance varies periodically as a function of the incident polarization angle, exhibiting the highest absorbance when the

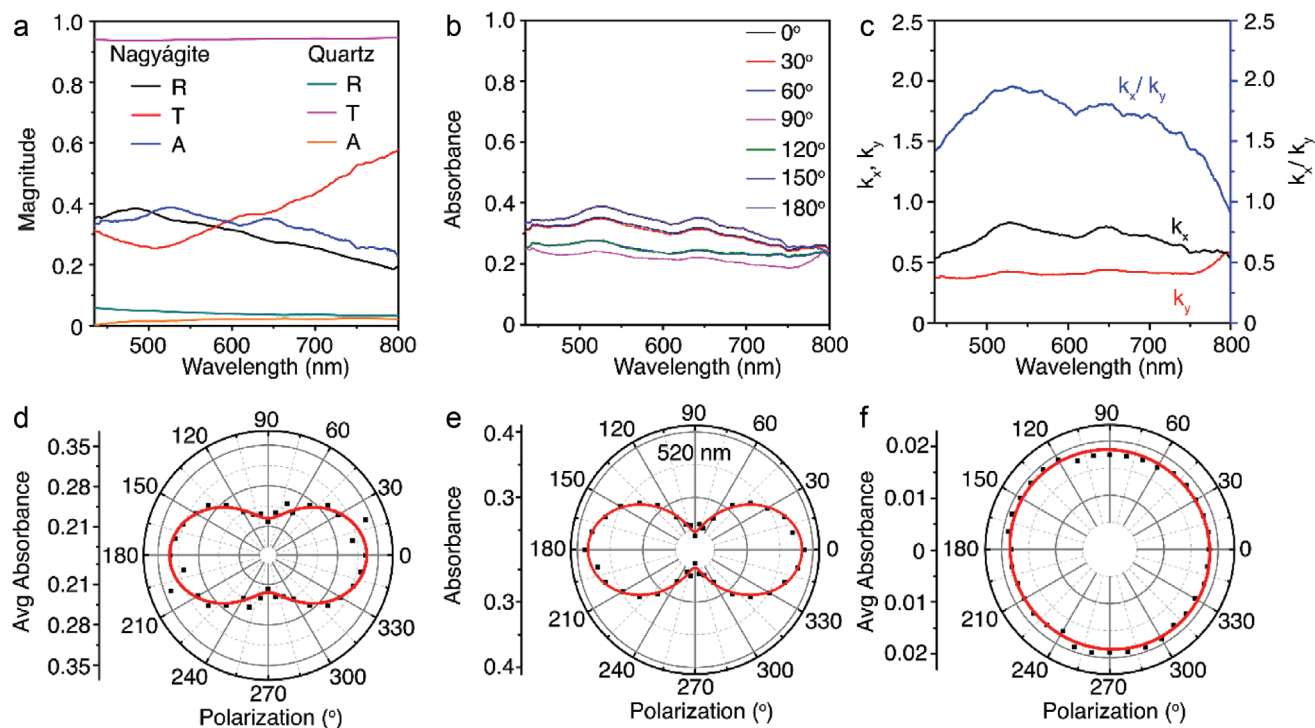


**Figure 5.** a) Measured reflectance ( $R$ ), transmittance ( $T$ ), and absorbance ( $A$ ) spectra from the 32 nm thick nagyágite flake and bare quartz substrate when the incident light is linearly polarized along the  $x$ -direction. b) Evolution of absorbance for a series of incident linear polarization angle between  $0^\circ$  and  $180^\circ$ . c) Imaginary part of the refractive index as a function of wavelength for two orthogonal linear polarizations along  $x$ -direction ( $k_x$ ) and  $y$ -direction ( $k_y$ ). The blue curve shows the  $k_x/k_y$  ratio. d, e) Polar plots of the evolution of average absorbance integrated over the wavelength range of 430–800 nm and the magnitude of absorbance at 520 nm as a function of the incident linear polarization angle. f) Polar plot of the evolution of average absorbance from bare quartz substrate within the wavelength range of 430–800 nm as a function of the incident polarization angle, showing an isotropic response.

incident light is polarized along the  $x$ -axis at  $\theta = 0^\circ$ . The imaginary part of the refractive index of the nagyágite flake is then extracted from the reflectance and absorbance measurements by using the equation<sup>[35]</sup>

$$k = \frac{\lambda}{4\pi d} \ln \left\{ \frac{2T}{[T^2 - (1-R)^2] + \left\{ [T^2 - (1-R)^2]^2 + 4T^2 \right\}^{1/2}} \right\} \quad (7)$$

The extracted  $k$  values as a function of wavelength are plotted in Figure 5c for the cases when the incident light is linearly polarized along  $x$ -direction ( $k_x$ ) and  $y$ -direction ( $k_y$ ). The evolution of  $k_x/k_y$  ratio, which is the quantification of linear dichroism in the nagyágite flake, is also plotted in Figure 5c. It shows that the  $k_x/k_y$  ratio is greater than 1 for most of the wavelength range and the value reaches 1.85 around 520 nm, manifesting a strong linear dichroism in the nagyágite crystal. The polar plot in Figure 5d further shows the angular dependence of average absorbance integrated over the whole wavelength range (430–800 nm) as a function of the incident linear polarization angle. The dipolar evolution of absorbance is fitted with a sinusoidal function of the form  $A(\theta) = A_x \cos^2 \theta + A_y \sin^2 \theta$ , showing the anisotropy ratio of absorbance  $A_x/A_y$  to be 1.47. In Figure 5e, the polar plot of the variation of absorbance at the wavelength of 520 nm as a function of the incident polarization angle is displayed, where the obtained  $A_x/A_y$  ratio is 1.58. To show that the linear dichroism effect is not due to the underlying quartz substrate, we plot the polarization-dependent evolution of average absorbance of bare quartz substrate in Figure 5f, where an isotropic response is observed. It is noted that for all the wavelengths, absorbance reaches the highest and lowest values

as the incident linear polarization aligning along  $x$ -direction at  $\theta = 0^\circ$  and  $y$ -direction at  $\theta = 90^\circ$ , respectively, which are exactly same as the crystal axes determined by the Raman measurement. Thus, the  $x$ -axis at  $\theta = 0^\circ$  and the  $y$ -axis at  $\theta = 90^\circ$  are identified as the crystal's  $a$ -axis and  $b$ -axis, respectively.

#### 2.4. Anisotropic Nonlinear Optical Response from Nagyágite Crystal

The in-plane anisotropy in crystal structure also induces anisotropic nonlinear optical properties of material. Hence, nonlinear harmonic generation is widely used for determination and characterization of the crystal symmetry. Therefore, the effect of structural anisotropy on the nonlinear optical properties of nagyágite is explored by polarization-dependent THG from nagyágite flakes. Figure 6a displays the transmission optical image of THG emission from a nagyágite flake, as illuminated by a 1560 nm fundamental laser with the spot size of 1.5  $\mu\text{m}$ . The thickness of the flake is estimated to be 265 nm from the AFM image in Figure 6b. First the crystal axes of the flake are determined from polarization-resolved Raman measurements. The polar plot of the Raman intensity variation of the parallel polarization component of the  $A_g$  mode at 137  $\text{cm}^{-1}$  in Figure 6c identifies that the crystal's  $a$ -axis is oriented along  $x$ -direction at  $\theta = 0^\circ$ . The recorded THG spectrum from the flake in Figure 6d shows an expected emission peak at 520 nm, which is exactly one-third of the fundamental wavelength. Figure 6e is the log-scale plot of the average third-harmonic (TH) power as a function of the average pump power of fundamental laser, where the cubic power-law dependence further confirms the THG process. Since nagyágite has a monoclinic

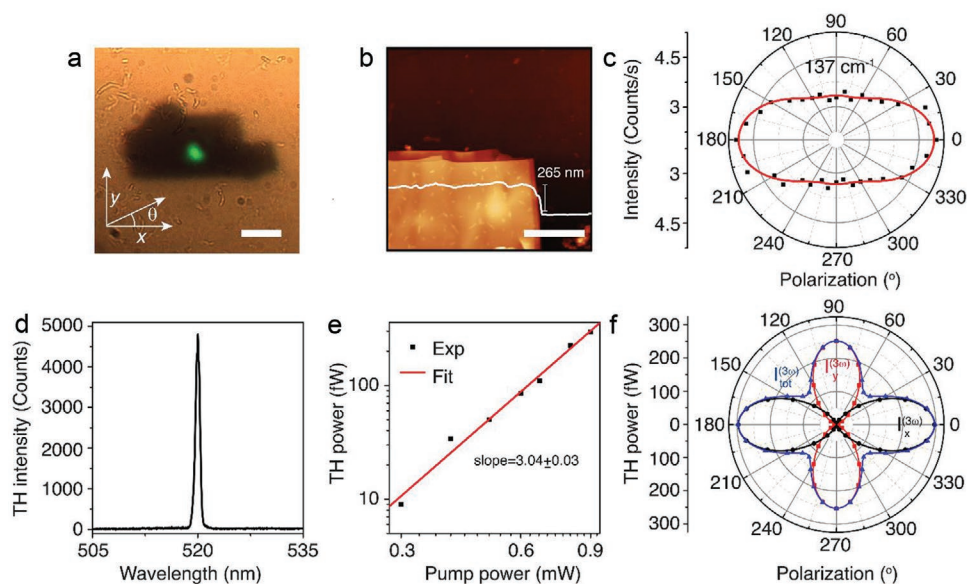


**Figure 6.** a) Transmission microscope image of THG emission from an exfoliated nagyágite flake. Scale bar is 5  $\mu\text{m}$ . b) AFM image of top right corner of the flake where the height profile in the inset shows that the flake is 265 nm thick. Scale bar is 2  $\mu\text{m}$ . c) Polar plot of the Raman intensity variation of the parallel polarization component of the  $A_g$  mode at 137  $\text{cm}^{-1}$  showing that the crystal's  $a$ -axis is oriented along  $x$ -direction. d) Recorded THG spectrum showing a peak wavelength at 520 nm, which is exactly one-third of the fundamental wavelength. e) Double log-scale plot of the measured average TH power as a function of incident pump power. f) Angular evolution of the average TH power as a function of the incident pump polarization angle. Black, red and blue data points are the measured data, while the solid curves are the corresponding theoretical fits.



crystal structure, the contracted form of the third-order susceptibility tensor can be written as<sup>[36]</sup>

$$\chi^{(3)} = \begin{bmatrix} \chi_{11} & 0 & 0 & 0 & 0 & \chi_{16} & 0 & \chi_{18} & 0 & 0 \\ 0 & \chi_{22} & 0 & \chi_{24} & 0 & 0 & 0 & 0 & \chi_{29} & 0 \\ 0 & 0 & \chi_{33} & 0 & \chi_{35} & 0 & \chi_{37} & 0 & 0 & 0 \end{bmatrix} \quad (8)$$

where the first subscript 1, 2, 3 refers to  $x$ ,  $y$ ,  $z$  respectively, and the second subscript signifies the following

$$\begin{matrix} xxx & yyy & zzz & yzz & yzy & xzz & xxz & xyy & xxy & xyz \\ 1 & 2 & 3 & 4 & 5 & 6 & 7 & 8 & 9 & 0 \end{matrix} \quad (9)$$

By considering the electric field of the fundamental beam at frequency  $\omega$  being linearly polarized at an angle  $\theta$  with respect to the  $x$ -axis, it can be expressed as  $\vec{E}^{(\omega)} = E_0 (\cos\theta \hat{x} + \sin\theta \hat{y})$ , with  $\hat{x}$  and  $\hat{y}$  being the unit vectors along  $x$ - and  $y$ -axis. No contribution from the components of  $\chi^{(3)}$  containing  $z$  terms is expected in the THG signal and hence only four non-zero elements of  $\chi^{(3)}$  as  $\chi_{11}$ ,  $\chi_{18}$ ,  $\chi_{22}$  and  $\chi_{29}$  will be contributing to the THG signal. Therefore, the  $x$ - and  $y$ -polarized components of the THG intensity can be written as

$$I_x^{(3\omega)} \propto (\chi_{11} \cos^3 \theta + 3\chi_{18} \cos\theta \sin^2 \theta)^2 \quad (10)$$

$$I_y^{(3\omega)} \propto (\chi_{22} \sin^3 \theta + 3\chi_{29} \sin\theta \cos^2 \theta)^2 \quad (11)$$

Figure 6f plots the evolution of the TH power as function of the incident linear polarization angle with respect to  $x$ -axis for the pump power of 0.9 mW. The black and red data points are the measured  $x$ - and  $y$ -polarized components of the TH power, while the blue data points show the measured total TH power. The solid lines are theoretical fits of the experimental data using Equations (10) and (11) which shows a good agreement between the theoretical prediction and the measurements. An anisotropic two-fold rotational symmetry is observed, where the maximum TH power occurs for the incident linear polarization at  $\theta = 0^\circ$  along the crystal's  $a$ -axis and the second maximum THG emission occurs at  $\theta = 90^\circ$  along the crystal's  $b$ -axis. The anisotropy ratio of the THG signal  $I_x^{(3\omega)}_{\theta=0^\circ} / I_y^{(3\omega)}_{\theta=90^\circ}$  is estimated to be 1.18, giving the  $\chi_{11}/\chi_{22}$  ratio of 1.09 according to Equations (10) and (11).

Finally, to assess the THG response of nagyágite, we estimate the effective scalar value of the third-order susceptibility  $\chi_{\text{eff}}^{(3)}$  which can be expressed as<sup>[37]</sup>

$$\chi_{\text{eff}}^{(3)} = \left( \frac{16\sqrt{n_3^2 + k_3^2} n_1^3 \epsilon_0^2 c^4 f_{\text{rep}}^2 W^4 \tau^2 \left[ \frac{\pi}{4 \ln 2} \right]^3 P^{(3\omega)}}{9\omega^2 d^2 P^{(\omega)^3}} \left( \frac{\left( \frac{4\pi^2 k_3^2 d^2}{\lambda_3^2} \right)}{e^{\frac{4\pi k_3 d}{\lambda_3}} - 2e^{\frac{2\pi k_3 d}{\lambda_3}} + 1}} \right)^{1/2} e^{\frac{4\pi k_3 d}{\lambda_3}} \right) \quad (12)$$

where  $P^{(3\omega)}$  represents the average TH power,  $d$  is the flake thickness,  $n_1$  and  $n_3$  are the real part of the refractive index of nagyágite at the fundamental wavelength  $\lambda_1$  and the

third-harmonic wavelength  $\lambda_3$ , while  $k_3$  is the imaginary part of the refractive index at  $\lambda_3$ . The parameters of the fundamental pump laser are given by spot size  $W = 1.5 \mu\text{m}$ , repetition rate  $f_{\text{rep}} = 80 \text{ MHz}$ , pulse width  $\tau = 90 \text{ fs}$ , and  $P^{(3\omega)}$  is the pump power. The value of  $k_3$  at  $\lambda_3 = 520 \text{ nm}$  is estimated to be 0.82 from the absorbance measurement. By considering the real part of the refractive index to be  $n_1 = n_3 = 3.5$ , the  $\chi^{(3)}$  value of nagyágite is estimated to be  $1.49 \times 10^{-20} \text{ m}^2 \text{ V}^{-2}$ .

### 3. Conclusions

In summary, we have demonstrated the mechanical exfoliation of natural vdW heterostructure nagyágite. We are able to achieve a flake thickness of 32 nm, which corresponds to only 21 pairs of layers of the vdW heterostructure. A better controlled mechanical exfoliation process and other exfoliation methods such as liquid phase exfoliation could allow the formation of 2D vdW heterostructures with even smaller thickness. The heterostructure is composed of alternating stacks of [Pb(Pb,Sb)S<sub>2</sub>] layers and single-atom thick [(Au,Te)] sheets. Through TEM analysis, we establish that the constituent lattices in the nagyágite crystal are commensurable with each other. By performing EDXS and XPS measurements, we further determine the chemical composition of the thin flakes of natural nagyágite to be [(Pb<sub>2.76</sub>Sb<sub>1.19</sub>)<sub>Σ=3.95</sub>S<sub>4</sub>][(Au<sub>0.63</sub>Te<sub>1.77</sub>)<sub>Σ=2.4</sub>]. The structural anisotropy in the thin nagyágite flakes are then characterized using polarization-resolved Raman spectroscopy. The effect of the structural anisotropy on the optical properties of the nagyágite crystal is further studied through polarization-dependent absorption measurements to demonstrate strong linear dichroism. It is shown that the principle crystal axes can be determined through the angular evolution of either the Raman intensity or the absorbance value. These results are not only important in the context of understanding the origin of optical anisotropy in natural vdW heterostructures but also can be harnessed to design future polarization-sensitive photo-detectors and modulators. Furthermore, it is shown that the crystal anisotropy in nagyágite can also be characterized by polarization-dependent THG measurements, giving that the TH power for the incident polarization along the  $a$ -axis is almost 1.18 times stronger compared to that along the  $b$ -axis. Moreover, the estimated bulk third-order susceptibility of nagyágite is found to be in the order of  $10^{-20} \text{ m}^2 \text{ V}^{-2}$ , which suggests that nagyágite could be a good material for realizing future nonlinear optical devices. In addition, the characterized and analyzed anisotropic Raman tensor, linear dichroism,

and third-order nonlinear susceptibility of nagyágite thin crystals indeed reveal the important intrinsic properties of this vdW layered material, which are of great importance for the

realization of many advanced linear and nonlinear optical applications.

## 4. Experimental Section

**Sample Preparation:** The quartz substrate was sonicated in deionized water, followed by acetone, and isopropanol. The thin nagyágite flakes were mechanically exfoliated from a natural mineral rock acquired from Săcărâmb, Deva, Hunedoara, Romania, using a Nitto tape (SPV 224) and then transferred onto the quartz substrate.

For the TEM measurement, thin nagyágite flakes were transferred onto a copper TEM grid by PMMA-assisted wet transfer method. First PMMA (950 kDa) was spin-coated (2000 rpm, 60 s) on the quartz substrate containing the thin flakes and baked at 120 °C for 2 min to facilitate the adhesion between nagyágite and PMMA. Next, the quartz was etched by immersing the sample in 3 M potassium chloride (KOH) solution for 1.5 to 2 h at 50 °C. Thereafter, the PMMA film containing the nagyágite crystals was washed with deionized water to remove the residual KOH. Then, the PMMA film was transferred on a TEM grid. The TEM grid covered with the PMMA film was left uncovered for drying out naturally. Finally, crystals were transferred on the TEM grid by washing out PMMA by dissolving it in acetone.

**Optical Setup:** For analyzing the Raman spectrum, a 632.8 nm He–Ne laser beam was focused on the nagyágite flake using a 40× objective lens (NA = 0.6). The linear polarization of the laser beam was determined using a linear polarizer and a rotating half-wave plate. The back-reflected light was collected by the same objective lens and directed toward a spectrometer (Horiba, iHR 520) using a beam splitter. The excitation laser was filtered out by placing a Rayleigh rejection filter (Semrock, LP02-633RE-25) in front of the spectrometer. The parallel and perpendicular polarization components of the Raman spectrum were analyzed using another linear polarizer before the spectrometer.

For the polarization-resolved absorption measurements, optical beam from a broadband white light source (Thorlabs, SLS201L, 360–2600 nm) was focused on the nagyágite flake using a 100× objective lens (NA = 0.7). The linear polarization of the incident light was controlled by rotating a linear polarizer before the objective lens. The reflection spectrum was recorded by collecting the back-reflected light from the sample using the same objective lens and directing it toward the spectrometer with a beam splitter, while the transmission spectrum was collected using another 100× objective lens. After normalizing both the reflection and transmission spectra with the source spectrum, reflectance ( $R$ ) and transmittance ( $T$ ) were obtained. Finally, the absorbance ( $A$ ) spectrum was obtained following the relation of  $A = 1 - R - T$ .

For THG measurements, a femtosecond laser pulse at the fundamental wavelength of 1560 nm (Calmar fiber laser, pulse width 90 fs, repetition rate 80 MHz) was passed through a linear polarizer and a half-wave plate, and then focused onto the nagyágite flake using a 40× objective lens (NA = 0.65). The transmitted THG emission from the nagyágite flake was collected by a 100× objective lens (NA = 0.7), and imaged by focusing onto a color charge-coupled device (CCD) camera. The transmitted fundamental pump beam is spectrally filtered using a low-pass filter. For the spectral characterization of the TH power, a spectrometer (Horiba, iHR 520) was used instead of the color CCD camera. The  $x$ - and  $y$ -polarized components of the THG signal were further analyzed using another linear polarizer before the spectrometer.

## Acknowledgements

The authors acknowledge support from the National Science Foundation under Grant No. DMR-1552871 and ECCS-1653032. The authors also thank Shatadru Chakravarty, Brian Porter, and Eric Bohannon for their help in acquiring TEM, XPS, and AFM data.

## Conflict of Interest

The authors declare no conflict of interest.

## Data Availability Statement

Research data are not shared.

## Keywords

nagyágite, optical anisotropy, Raman scattering, third-harmonic generation, van der Waals heterostructure

Received: June 30, 2021

Revised: October 8, 2021

Published online:

- [1] M. Zeng, Y. Xiao, J. Liu, K. Yang, L. Fu, *Chem. Rev.* **2018**, *118*, 6236.
- [2] S. Das, J. A. Robinson, M. Dubey, H. Terrones, M. Terrones, *Annu. Rev. Mater. Res.* **2015**, *45*, 1.
- [3] D. Akinwande, C. J. Brennan, J. S. Bunch, P. Egberts, J. R. Felts, H. Gao, R. Huang, J.-S. Kim, T. Li, Y. Li, K. M. Liechti, N. Lu, H. S. Park, E. J. Reed, P. Wang, B. I. Yakobson, T. Zhang, Y.-W. Zhang, Y. Zhou, Y. Zhu, *Extreme Mech. Lett.* **2017**, *13*, 42.
- [4] B. Aïssa, N. K. Memon, A. Ali, M. K. Khraisheh, *Front. Mater.* **2015**, *2*.
- [5] M. Coroş, F. Pogăcean, L. Măgeruşan, C. Socaci, S. Pruneanu, *Front. Mater. Sci.* **2019**, *13*, 23.
- [6] S. Manzeli, D. Ovchinnikov, D. Pasquier, O. V. Yazyev, A. Kis, *Nat. Rev. Mater.* **2017**, *2*, 17033.
- [7] W. Choi, N. Choudhary, G. H. Han, J. Park, D. Akinwande, Y. H. Lee, *Mater. Today* **2017**, *20*, 116.
- [8] B. Li, C. Lai, G. Zeng, D. Huang, L. Qin, M. Zhang, M. Cheng, X. Liu, H. Yi, C. Zhou, F. Huang, S. Liu, Y. Fu, *Small* **2019**, *15*, 1804565.
- [9] A. K. Geim, I. V. Grigorieva, *Nature* **2013**, *499*, 419.
- [10] K. S. Novoselov, A. Mishchenko, A. Carvalho, A. H. Castro Neto, *Science* **2016**, *353*, aac9439.
- [11] R. Ribeiro-Palau, C. Zhang, K. Watanabe, T. Taniguchi, J. Hone, C. R. Dean, *Science* **2018**, *361*, 690.
- [12] F. Withers, O. Del Pozo-Zamudio, A. Mishchenko, A. P. Rooney, A. Gholinia, K. Watanabe, T. Taniguchi, S. J. Haigh, A. K. Geim, A. I. Tartakovskii, K. S. Novoselov, *Nat. Mater.* **2015**, *14*, 301.
- [13] W. Chen, Z. Sun, Z. Wang, L. Gu, X. Xu, S. Wu, C. Gao, *Science* **2019**, *366*, 983.
- [14] Y. Liu, N. O. Weiss, X. Duan, H.-C. Cheng, Y. Huang, X. Duan, *Nat. Rev. Mater.* **2016**, *1*, 16042.
- [15] M. Velický, P. S. Toth, A. M. Rakowski, A. P. Rooney, A. Kozikov, C. R. Woods, A. Mishchenko, L. Fumagalli, J. Yin, V. Zólyomi, T. Georgiou, S. J. Haigh, K. S. Novoselov, R. A. W. Dryfe, *Nat. Commun.* **2017**, *8*, 14410.
- [16] A. J. Molina-Mendoza, E. Giovanelli, W. S. Paz, M. A. Niño, J. O. Island, C. Evangelini, L. Aballe, M. Foerster, H. S. J. van der Zant, G. Rubio-Bollinger, N. Agrait, J. J. Palacios, E. M. Pérez, A. Castellanos-Gomez, *Nat. Commun.* **2017**, *8*, 14409.
- [17] R. Frisenda, G. Sanchez-Santolino, N. Papadopoulos, J. Urban, M. Baranowski, A. Surrente, D. K. Maude, M. Garcia-Hernandez, H. S. J. van der Zant, P. Plochocka, P. San-Jose, A. Castellanos-Gomez, *Nano Lett.* **2020**, *20*, 1141.
- [18] Y. Niu, J. Villalva, R. Frisenda, G. Sanchez-Santolino, L. Ruiz-González, E. M. Pérez, M. García-Hernández, E. Burzurí, A. Castellanos-Gomez, *2D Mater.* **2019**, *6*, 035023.

- [19] R. P. N. Tripathi, J. Gao, X. Yang, *Sci. Rep.* **2021**, *11*, 8510.
- [20] J. Li, K. Yang, L. Du, J. Yi, J. Huang, J. Zhang, Y. He, B. Huang, L. Miao, C. Zhao, S. Wen, *Adv. Opt. Mater.* **2020**, *8*, 2000382.
- [21] C. A. Francis, A. J. Criddle, C. J. Stanley, D. E. Lange, S. S'how, J. G. Francis, *Can. Mineral.* **1992**, *30*, 1039.
- [22] L. Fang, J. Im, C. C. Stoumpos, F. Shi, V. Dravid, M. Leroux, A. J. Freeman, W.-K. Kwok, D. Y. Chung, M. Kanatzidis, *J. Am. Chem. Soc.* **2015**, *137*, 2311.
- [23] L. Bindi, W. H. Paar, *Eur. J. Mineral.* **2017**, *29*, 673.
- [24] W. Haidinger, *Handbuch der Bestimmenden Mineralogie*, Braumüller & Seidel, Wien **1845**.
- [25] C. Ciobanu, N. Cook, A. Pring, G. Damian, N. Căpraru, *Mineral. Petrol.* **2008**, *93*, 273.
- [26] H. Chen, J. He, C. D. Malliakas, C. C. Stoumpos, A. J. E. Rettie, J.-K. Bao, D. Y. Chung, W.-K. Kwok, C. Wolverton, M. G. Kanatzidis, *J. Am. Chem. Soc.* **2019**, *141*, 7544.
- [27] H. Effenberger, W. H. Paar, D. Topa, F. J. Culetto, G. Giester, *Am. Mineral.* **1999**, *84*, 669.
- [28] G. D. Smith, S. Firth, R. J. H. Clark, M. Cardona, *J. Appl. Phys.* **2002**, *92*, 4375.
- [29] R. Parize, T. Cossuet, O. Chaix-Pluchery, H. Roussel, E. Appert, V. Consonni, *Mater. Des.* **2017**, *121*, 1.
- [30] P. Sereni, M. Musso, P. Knoll, P. Blaha, K. Schwarz, G. Schmidt, *AIP Conf. Proc.* **2010**, *1267*, 1131.
- [31] H. Sar, J. Gao, X. Yang, *Sci. Rep.* **2020**, *10*, 14282.
- [32] L. Zhou, S. Huang, Y. Tatsumi, L. Wu, H. Guo, Y.-Q. Bie, K. Ueno, T. Yang, Y. Zhu, J. Kong, R. Saito, M. Dresselhaus, *J. Am. Chem. Soc.* **2017**, *139*, 8396.
- [33] H. B. Ribeiro, M. A. Pimenta, C. J. S. de Matos, R. L. Moreira, A. S. Rodin, J. D. Zapata, E. A. T. de Souza, A. H. C. Neto, *ACS Nano* **2015**, *9*, 4270.
- [34] M. Li, Y. Wu, T. Li, Y. Chen, H. Ding, Y. Lin, N. Pan, X. Wang, *RSC Adv.* **2017**, *7*, 48759.
- [35] X. Yang, C. Hu, H. Deng, D. Rosenmann, D. A. Czaplewski, J. Gao, *Opt. Exp.* **2014**, *21*, 2631.
- [36] X.-l. Yang, S.-w. Xie, *Appl. Opt.* **1995**, *34*, 6130.
- [37] N. Youngblood, R. Peng, A. Nemilentsau, T. Low, M. Li, *ACS Photonics* **2017**, *4*, 8.